INFRARED EMITTING PBS NANOCRYSTALS THROUGH MATRIX ENCAPSULATION

Geethika Kaushalya Liyanage

A Thesis

Submitted to the Graduate College of Bowling Green
State University in partial fulfillment of
the requirements for the degree of

MASTER OF SCIENCE

August 2014

Committee:

Mikhail Zamkov, Advisor

Haowen Xi

Liangfeng Sun

ABSTRACT

Mikhail Zamkov, Advisor

Colloidal semiconductor nanocrystals are becoming widely used materials in developing high performing light emitting devices in the Infrared region. The ability of tuning their properties at the colloidal stage and easy-low-cost processing of these Quantum Dot solutions in to nanocrystal solid devices makes them a perfect candidate in the device engineering process. One of the main challenges that present methods of making Infrared emitting thin film devices face is that both quantum yield efficiency and stability is compromised when processing them from colloidal stage to the solid state. The proposed method provides a better solution to this problem allowing a better assembly of Infrared emitting PbS nanocrystals encapsulated into an all inorganic matrix of wide band gap CdS. The newly proposed Semiconductor Matrix Encapsulation Nanocrystal Array (SMENA) method provides a better passivation in the PbS surfaces which can be optimized to reduce the non-radiative exciton decaying processes preserving the emission characteristics of the film. Due to the strong localization of the electrical charges, the films fabricated using modified SMENA method shows a bright emission yield compared to the current reported techniques. In addition to a high emission quantum yield, fabricated films exhibit excellent thermal and chemical stability, which avails their integration into solid state IR emitting technologies.

In the loving memory of my mother

ACKNOWLEDGMENTS

First of all, I would like to thank my advisor Dr. Mikhail Zamkov for his enormous support and guidance that helped become a good researcher and a well qualified graduate student. I feel myself fortunate to work as a part of Zamkov research group that paved the path to pursue in the field of Nanoscience. Also, I am thankful to my group members, Pavel Morov, Natalia Kholmicheva, Prakash Upretty, Ebin Bastola and Upendra Rijal, for helping me to complete this project. Also I gratefully acknowledge Kamal Subedi and Sergii Yakunin and Dr. Maksym V. Kovalenko for supporting me with the characteristic measurements.

I would like to convey my gratitude to Dr. Haowen Xi and Dr. Liangfeng Sun, my committee members, for spending their valuable time for my benefit.

Furthermore, I am extremely thankful for the support and emotional strength I had from my late mother, Shriyani Wickramasingha, father, Piyasena Liyanage, Sisters, Gayathri Liyanage and Achinthya Liyanage. Your love, care and support made everything possible in my life

Finally, my special thanks go with tremendous respect to Dr. Lewis Fulcher, my graduate coordinator, who guided me throughout my master's degree and all the faculty and staff members in the department of Physics and Astronomy at BGSU.

TABLE OF CONTENTS

LIST OF FIGURES

LIST OF TABLES

CHAPTER 1: INTRODUCTION

1.1 Background

Semiconductor nanocrystals have become widely studied materials emerging new technologies in chemistry, physics, materials engineering and recently in the fields of medicinal sciences and bioengineering. The confinement of the excitons in three dimensions gives these semiconductor nanocrystals, "quantum dots" (QDs), properties between its bulk form and of the single molecules[1] allowing them to be used in broad range of applications in making light emitting devices (LEDs)[2-9], lasers[10-12], solar cells[13-19], and other electronic devices[20-24].

The extensive use of these QDs was mainly due to the ease of controlling the properties of these nanocrystals depending on the materials and architecture, and the flexibility of varying the inbuilt properties during the growth. These alterations were handled according to the application by changing the size, shape and the structure of these QDs via changing the temperature conditions, precursors and solvents. Another important factor for the wide-range use of these nanocrystals is the simple deposition techniques on thin films rather than the conventional deposition techniques that use high temperature and high vacuum systems, which makes these QDs ideal in making cost effective devices.

1.2 Core/shell structure

The preservation of the optical characteristics of these QDs associated with the colloidal phase is a crucial fact when determining the efficiency of the devices that are to be produced. Typically, QDs consist with an inorganic core of several hundred atoms surrounded by surface ligands. Even with this passivation by ligands, QDs, shows a significant amount of trap states driving the percentage of the non-radiative de-excitation for the photo-generated charge carrier to

a higher level, which significantly affect the quantum yield[25]. One method to reduce the effect of surface trapping in QDs is to use a passivation with a core/shell structure of these nanocrystals during their growth has which enhance the efficiency improving the fluorescence and providing a better stability.

The appropriate use of the materials during the synthesis allows these QD core/shells to create three different types of alignments Type I, Type II or reverse Type I of the band structures at the hetero-interface of the materials. These types can be used in desired applications over a large spectral range according to the different mechanisms that the photo-induced charges undergo.

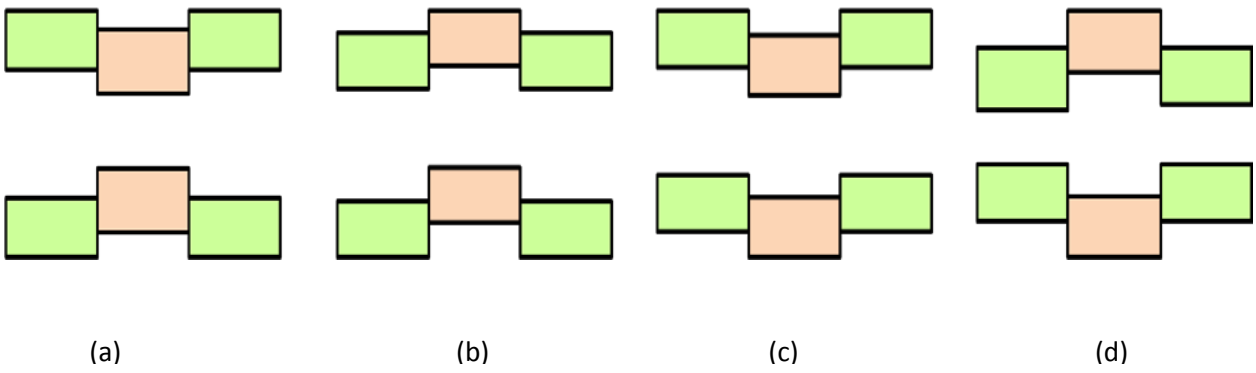

Figure 1.1 – Alignment of energy levels of different core/shells structures. (a) Type I hetero-structure, (b) & (c) Type II hetero-structure and (c) Reverse Type I hetero-structure.

In Type I alignment, the band gap of the core lies in between the band gap of the shell and vice-versa in Reverse Type I, which drives the recombination of the photo-excited charges enhancing the optical properties of the material either in core or the shell. The band gap of the shell of Type II alignment is mostly smaller than of the core material providing a complete or

partial confinement of the charges depending on the thickness of the shell; thus, opening applications in photovoltaics, catalysis and other electronic devices.

When fabricating thin-film devices, these core-shell structures have more control in fusing the films in with fewer defects which improves the efficiency and the performance of the films[25].

1.3 Nanocrystal light emitting materials

The size dependent optical properties of these QDs have been extensively researched to find bright fluorophore, which are more stable in solution state as well as in the solid state[26]. Different methods of production of light emitting materials have been reported over the past decades where the abovementioned Type I core/shell structures were frequently used in making high luminescent nanocrystaline materials. By choosing correct materials of the desired emission wavelength , scientist have presented many methods in fabricating better light materials with the emission in the visible and UV ranges[27-31].

1.4 Infrared emitting materials

Nanocrystal materials have created a greater impact on the opto-electronic device fabrication challenging the current technologies. The use of these nanocrystaline materials to emit Infrared (IR) has become more dominant in many fields ranging from telecommunication to medicinal science. The interest in IR nanocrystal materials started with the necessity of optical amplification in the telecommunication media, ranging from 1.3 μm to 1.7 μm with a main focus on the C-band around 1.55μm[32]. On the other hand, the use of near-IR nanocrystals in medicinal sciences has become more rapidly used for the biomedical imaging of the live tissues. However, the research on discovering better IR emitting materials in spectral range from 800nm

to 2000nm has a great impact in these technologies as the present work in that area is limited[26]. Most of the organic or inorganic materials that are presently used in building these devices confront an inability produce IR emission in the required range as the quantum yield of the emission is considerably low compared to that of the light emitting materials in visible range.

In contrast to these materials, the use of these QDs or semiconductor IR emitting nanocrystals materials have become promising materials in the direction of making better IR light emitting devices. Use of Ag_2Te/ZnS core/shell near IR emitting materials was reported by Chen et al., [33] with a PL emission range from 900nm to 1400nm with a relative quantum yield up to 5.6%, and Zhu et al.,[34] shows optical emission around the same range using Ag_2Se. But recent studies show that using Pb^{2+} chalcogenide (PbS, PbTe and PbSe) semiconductor nanocrystals scientists were able to obtain a better quantum confinement that the emission quantum yield was enhanced up to 50%, with contrast to the efficiency of 3-5% using traditional Ga, Si bulk semiconductor devices[26, 35, 36].

For example, the exciton Bohr radius of PbSe is 46nm and it is 20nm for the PbS[37]. In order to have better quantum confinement, the radius of the synthesized QDs of these Pb^{2+} chalcogenids should be smaller than these Bohr radius values which allow us to have better optical transition at the desired range from 1μm up to 3.35 μm [37]. Choosing a better core/shell structure by using wide band gap material for the shell material will enhance this efficiency even to a higher value as excitons will be more confined to the core allowing an efficient de-excitation. Apart from the better efficiency, these semiconductor nanocrystals are stable at colloidal state, providing an inexpensive method of making better thin-films by processing those solutions.

1.5 IR emitting films

The development of competitive IR emitting devices is largely dependent upon the ability to assemble them into stable structures or matrices that will preserve the monodispersity of the used materials. Apart from the bright band gap emission, these solid matrices should demonstrate a significant thermal stability as well as a better chemical stability. Also, in order to utilize them as waveguides, these matrices should also contain a high refractive index. Additionally, these devices should acquiring high QD loading factor (filling factor) which is essential in obtaining large gain magnitude.

The existing matrix encapsulation strategies relying on organic polymer mixes[38-42] are noticeably successful in transforming these nanoparticle solutions into thin films that can be implemented as devices, but attaining a considerable nanoparticle packing density (filling factor) and the phase separation of the polymer/semiconductor layers has been a challenge.

The method proposed by Sundar *et al.,* [43] and Petruska *et al.*, [44] by introducing sol-gel titania matrices have helped overcoming some of these challenges. By the use of these titania functional groups transferring directly to alcohol–terminated amine ligands, increasing the filling factor and the preservation of the monodispersity. Also using this method, a high volume loading up to 20% was reported along with an improved thermal stability in the TiO_x-incorporated CdSe NC films[44]. However, even with a higher filling factor, the ligand termination at the NC surface still generates poor stability and low quantum yield efficiency when incorporating these QDs in films.

More recently, a novel matrix encapsulation method was reported by Kovalenko *et al.*, [35] which focus on embracing PbS/CdS core/shells in to a solid metal complex of As_2S_2 amorphous

matrix. The $-As_2S_3$ matrix with a high refractive index and with an optical insulation ranging from near IR to mid IR optical region acts as a good nonlinear optical waveguide material. This method have enable a route to produce highly stable, all-inorganic nanoparticle films with a large refractive index approximately 5.1 which leads to a significant increase in the conductivity of the film. The low temperature solution processing technique provides an ability to deposit such nanocrystals virtually on any material[35]. .

Even with the accomplishments and the considerable progress in fabricating stable nanocrystal thin film materials that have been made in the recent years, the reported methods still suffer from several shortcomings. The significant reduction of the quantum yield and the drop of the fluorescence lifetime of the solid form of these materials have always been a major drawback when trying to imprint the QDs to solid matrices. For example, the fluorescence quantum yield of tethered CdSe nanocrystals in to Titania matrix was reported to decrease from 70% to an average value close to 10%[44]. Similarly, the proposed method by Kovalenko *et al*.,[35] the longest fitted fluorescence lifetime of the PbS/CdS-As_2S_3 films was dropped down to ~530ns compared to ~2600ns obtained when the PbS/CdS nanocrystals in tetrachloroethylene (TCE) solution which is a 4.9 fold difference in upon the fusion into a glassy matrix.

1.6 Proposed Matrix Encapsulating method

Having these aforementioned challenges faced by the recent encapsulation methods, it has been clearly identified that the quenching of the fluorescence in these QDs in films mostly occurs due to the non-radiative decay pathways. Apart from the radiative de-excitation of the charges which if longer, two distinct processors can be stated significant when considering the non-radiative decay of the excitons. Among the two processors, the transfer of energy or the

excited charges from one QD in the film to the nearest or to QD near the vicinity can lead create 'dark' excited states. The loss of charges or energy can directly affect the radiative recombination reducing the quantum yield efficiency. On the other hand, due to the interfacial defects at the nanocrystal-matrix hetero-interface or the trapping of charges on dangling bonds can create another non-radiative decay of charges.

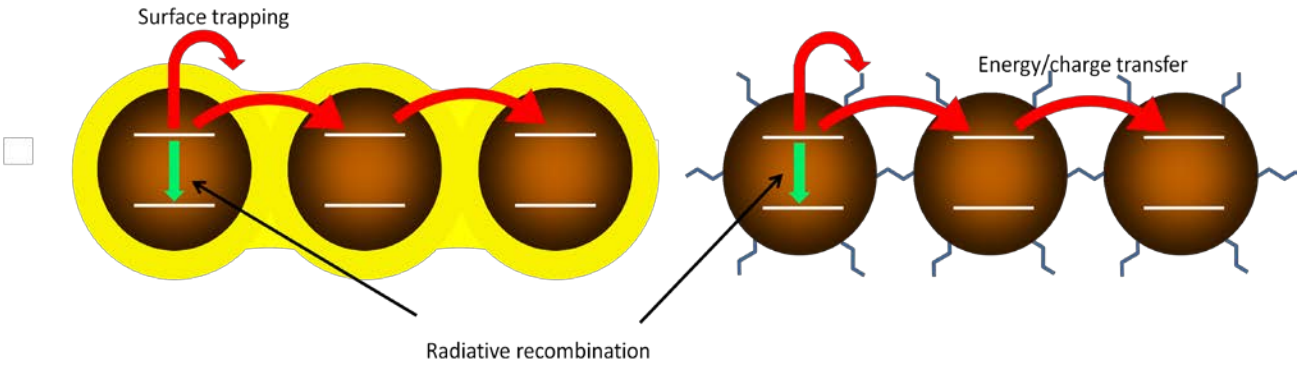

Figure 1.2 – Charge and energy dissociation processors of a photo-excited QD

The significant process from above two mechanisms, the charge transfer process of the excited charges in an encapsulated system, was shown to be almost exponential with the interparticle distance (R_{edge}) and the height ($\sqrt{\Delta E}$) of the potential barrier between two neighboring nanocrystals.[45] There for this charge transfer process can be restrained by using a core/shell structured QDs using a wide band gap material as the shell material or by increasing the interparticle distance to a sufficient value so that the hopping of charges between the embedded QDs will be suppressed.

Even with ensuring the suppression of the charge transfer to adjacent nanocrystals, trapping of the excited charges at the surface intermediate states still creates a challenging problem in the

embedded nanocrystals. In the titania matrices, the long organic ligands were used to lower the density of trap states at the surfaces of the nanocrystals while fusing them in the films[44]. But the emission of the nanocrystals was affected when the surface ligands were desorbed from the nanocrystals due to the thermal and electrical stimulation. The embedded nanocrystals in a glassy matrix provide a better solution to this problem reducing the density of trap states[35]. However, the fusion of the nanocrystals in to the glassy matrix still causes an imperfect surface passivation[31].

As for an ideal matrix encapsulated system of nanocrystals should have a high chemical and thermal stability and should consist with well bonded surface passivation layer. The proposed methodology demonstrates the assembling of IR emitting PbS nanocrystals via hot injection methods and encapsulation of them in to all inorganic matrices. The surfaces of the core nanocrystals structure were completely passivated using wide band gap shell of CdS, replacing the organic ligands. The heteroepitaxial passivation of the PbS nanocrystals surfaces enables the better quantum confinement of the generated excitons providing a better shield from the external environment and reduces the density of dangling bonds with one-to-one capping of surface ions compared to the traditional ligand passivation strategies that depends on the donor-acceptor interaction. It was observed that the encapsulated nanocrystal structure demonstrated a considerably improved emission quantum yield compared to the previously reported values and an excellent chemical and thermal stability.

CHAPTER 2: EXPERIMENTAL SECTION

2.1 Chemicals

oleic acid (OA, 90% Aldrich), 1-octadecene (ODE, 90% Aldrich), sulfur (S, 99.999% Acros), bis(trimethylsilyl) sulfide (TMS_2, Aldrich, synthetic grade), lead(II) oxide powder (PbO, 99.999% Aldrich), cadmium oxide (CdO, 99.99%, Aldrich), isopropanol (anhydrous, 99.8% Acros), hexane (anhydrous, 95% Aldrich), cadmium acetate dihydrate ((CH3COO)2Cd·2H2O, 3-mercaptopropionic acid (3-MPA, 99% Alfa Aesar), chloroform (anhydrous, 99%, Aldrich), 98%, Acros), sodium sulfide nonanhydrate (Na2S·9H2O, 98% Alfa Aesar), ethanol (anhydrous, 95% Aldrich), acetone (anhydrous, Amresco, ACS grade), toluene (anhydrous, 99.8% Aldrich), methanol (anhydrous, 99.8% Aldrich), octane (anhydrous, 99% Aldrich) were used for all the reactions and procedures as received without further purification. For thin film fabrication, glass substrates (Corning Microscope Slides, 0.96-1.06 mm, 0215 Glass) were obtained from Corning Inc.

2.2 Methods

2.2.1 Synthesis of PbS nanocrystals

The colloidal stage of the PbS nanocrystals were prepared according to the procedure described in Hines *et al*.[46] An amount of 0.49 g of lead(II) oxide powder (PbO) was mixed with 18 mL of 1-octadecene (ODE) and desired amount of oleic acid (OA) (1-16 mL of OA was used depending on the required size of the PbS nanocrystal grown) in a three neck flask and the mixture was degassed at 120°C for 2 hours to dissolve the PbO while overcoming any unwanted contamination. The degassed mixture containing PbO was then carefully switched to Argon (Ar)

and the temperature was increased to 135 °C. At the same time the Pb precursor solution was set to degas, 10 mL of ODE was also degassed for two hours at 120°C.The degassed ODE was switched to Ar and cooled to room temperature and 0.21 ml of bis(trimethylsilyl) sulfide (TMS_2) was carefully added into the flask. After letting to stir for one minute, the well mixed TMS_2/ODE mixture was quickly injected to the flask with the Pb-precursor at 135°C. After addition of TMS_2/ODE mixture, the reaction was continued to heat at 135°C for 0-5 minutes depending on the required size of the PbS nanocrystals (longer cooking time at 135°C results larger nanocrystals). Then the reaction was quenched by removing the heating of the flask and placing it in an iced water bath.

The cleaning of the prepared nanocrystals was performed after letting the mixture to be cooled to room temperature. The nanocrystals were precipitated by centrifuging with distilled acetone. The residue was saved by pouring off the liquid and again it was re-dispersed in toluene. The cleaning process of precipitation and re-dispersion was performed 2-3 times and finally the PbS nanocrystals were re-dissolved in 4-5 mL of hexane.

For a typical fabrication of PbS nanocrystal with a diameter of 3.0 nm (exciton absorption peak approximately at 950 nm), the PbS precursor was contained with 1.5mL of OA and the heating time was 1 minute. For nanocrystals with a diameter of 3.85nm (exciton absorption peak at 1140 nm), 10 mL of OA was used in the mixture and the growth time was 2 minutes. For larger diameters approximately 6.0 nm (absorption peak at 1700nm) PbS nanocrystals, 15 mL of OA was used in the mixture and the heating was continued for 4 minutes.

2.2.2 Synthesis of PbS/CdS core/shells through cation exchange

The CdS shell growth around the PbS cores were performed using the cation exchange method illustrated in Pietryga *et al.*[26] In a typical synthesis of making CdS shell, 0.95g (7.6mmol) of cadmium (II) oxide powder (CdO) was mixed with 18 mL of ODE and 10 mL of OA in a three-neck 50 ml flask and the mixture was heated at 240 °C under Ar flow, until the red solution was tuned clear. Upon all the CdO was turned to Cd-oleate, the temperature was decreased to 130 °C. At the same time, in a 25 mL three-neck flask under Ar flow, 4 mL of PbS seeds (cores) dissolved in hexane was heated at 100 °C for 2 minutes to remove the solvent (hexane). At the temperature of 135 °C, the heated PbS nanocrystals were added to the Cd-oleate solution with vigorous stirring. Then, the mixture was heated at 135 °C for 7minutes (The desired shell thickness was determined by using a proper temperature at a range from 120 °C to 160 °C). The flask was placed in an iced-water bath to quench the further growth of the shell.

The cleaning process of synthesized PbS/CdS nanocrystals was done by adding ethanol and centrifuging at 5000RPM. The clear liquid was discarded and the residue was re-dispersed in toluene. The steps were repeated two times to further purification and the final precipitate was dissolved in a 4-5 mL of hexane.

The growth of the shell around PbS nanocrystals were monitored by the shifting of the exciton absorption peak to the blue region compared to its original position. Assuming the size of the PbS original core remains unchanged, the subtraction of the difference of the core size was used to determine the thickness of the shell after exchanging the Pb^{2+} ions with the Cd^{2+}. This method provides a better accuracy of the shell growth than the TEM images.

With the above ratios of precursors and the growth temperature, a 330 nm blue shift of the exciton absorption peak was measured. The estimated CdS shell thickness was calculated to be 0.8 nm. For thick shell of CdS, higher ratios of ODE/OA, higher temperatures and longer reaction time was used.

2.2.3 Synthesis of CdS nanoparticles

The synthesis of CdS cores was adapted from the method reported in Yu *et al.*[47] In a Cd-precursor was prepared by mixing 0.0384 g (0.3 mmol) of CdO with 1 ml OA and 12 ml ODE in a 50 ml 3-neck flask and heating the mixture at 240 ºC under inert conditions until the formation of Cd-oleate solution (until the solution turned colorless). Then, the temperature was raised to 250 ºC. At the same time, the sulfur precursor was prepared by mixing 0.0048 g (0.15 mmol) sulfur powder 5ml of ODE and heating the mixture at 120ºC until the powder was dissolved completely. Then the sulfur precursor was quickly injected to Cd-oleate solution and the reaction was stopped by removing the heating after 5-9 minutes. The desired size of the CdS seeds was determined by monitoring the exciton absorption peak and the final seeds had a diameter from 3.5nm – 4.5 nm depending on the reaction time of the mixture.

The first step of the purification of the synthesized CdS cores involved with the methanol/hexane extraction to remove the unreacted Cd-oleate from the solution. Then the CdS seeds in the extracted yellow solution were precipitated by the addition of ethanol and centrifuging at 5000RPM for 10 minutes. The colorless solution was discarded and the yellow, oily precipitate was re-dispersed in 4-5 mL of hexane and stored in a dark place for the thin film production.

2.2.4 Preparation of the glass substrate

For the preparation of the nanocrystal coated films on glass slides (dimensions of 2.5 cm x 2.5 cm), the substrates were cleaned and dried for the optimal performance. First the substrates were washed with Alconox detergent in warm water and rinsed with deionized water. Afterward, the substrates were sonicated in methanol, acetone and finally in isopropanol for 5 minutes and left to dry under inert conditions.

2.2.5 Processing solution of PbS/CdS nanocrystals for thin film fabrication

The fabrication of the all-inorganic thin films of PbS/CdS nanocrystals was done by a layer-by-layer deposition method adapted from Kinder *et al.*[48] All the steps of the reported Semiconductor Matrix Encapsulation Nanocrystal Array (SMENA) methodology was performed inside the glove box with inert conditions to avoid unwanted oxidation in the films.

As the first step of the deposition technique, the PbS/CdS nanocrystals (in hexane) were added drop wise (4-5 drops) on to FTO glass substrate while spinning at 5800 RPM rate. The addition of the core/shells was carefully done until the substrate was fully covered and then allowed to dry. OA ligands on the spin coated core/shells were then exchanged to 3-mercaptopropionic acid (MPA) by adding 10 drops of a solution mixture containing 1:4 MPA/methanol, as completely covering the substrate. After allowing the glass to stand for five seconds, it was spun at 5800RPM for 10 seconds. The unexchanged, excess MPA ligands in the film were rinsed using 10 drops of methanol followed by spinning at 2500 RPM for 10 seconds. And as the final step of the cycle, the film was washed with 10 drops of hexane and spun at 2500 RPM for 10 seconds.

After two successful layers, the film was annealed at 150 °C for 15 minutes to evaporate the exchanged MPA ligands in the core/shells and for the better fusion of the encapsulated nanocrystals. For a typical thin film that was used for the measurements, 4-6 layers were deposited on the FTO glass substrate to have a thin film with a 300 nm thickness.

The modified SMENA films used in this project were fabricated with an addition of synthesized CdS cores along with the PbS/CdS cores/shell when spin coating the films. The proportion of the added PbS/CdS and CdS in a film was calculated by dividing the optical densities of the first exciton absorption peaks of the solutions. For PbS/CdS the considered peak was 850nm-900nm and for CdS seeds the peak was 430 nm. The final ratios of the nanocrystals were calculated using the TEM data obtained from the same solutions.

2.2.6 In-filling of nanocrystal solids pores with CdS

The fabricated nanocrystal films were processed through Successive Ionic Layer Adsorption and Reaction (SILAR) method adapted from Pathan *et al.,* [49] to fill the pores between the QDs with additional CdS. The deposition technique involves the soaking of SMENA films in prepared solutions of Cd^{2+} and S^{2-} in methanol. 0.113g of cadmium acetate dihydrate ($(CH_3COO)_2Cd.2H_2O$) was dissolved in 20 mL of methanol solution to prepare the required cadmium bath and the sulfur bath was prepared by dissolving 0.098g of sodium sulfide nonanhydrate (Na2S·9H2O) in 20 mL of methanol.

For the pore-filling process, first the prepared thin films were dipped in the Cd^{2+} solution for 1 minute followed by rinsing with pure methanol for 1 minute and then dipped in the S^{2-} solution for 1 minute again followed by the rinsing in pure methanol for 1 minute to complete one cycle. For a film with a high quality and good performance, 2-10 pore-filling cycles were

performed and according to the number of monolayers of CdS needed. For better fusion of the adsorbed CdS in the films, the films were annealed at 150 °C under inert conditions for 15 minutes.

2.3 Characterization

All the exciton absorbance data were measured using Simadzu UV-3600 UV-vis-NIR and CARY 50 scan spectrophotometers. The Photoluminescence (PL) data were measured using a Jobin Yvon Fluorolog FL3-11 fluorescence spectrophotometer and using a custom-built PL spectroscopy apparatus. The apparatus consisted with an Acton SP-2357 Monochromator (Princeton Instrument), an Argon ion laser Reliant 150M (Laser Physics) and with an IR detector PDA30G (Thorlabs).

The JEOL 3011UHR (operated at 300 kV) and 2010 transmission electron microscope (200 kV) was used to obtain High-resolution transmission electron microscopy (HR-TEM) measurements. The preparation of the sample for the TEM measurements we done by scrapping a small part of nanocrystal films, dissolved in toluene by sonication and deposited on to a carbon-coated copper grip and allowing it to dry. To obtain the colloidal state TEM images, a diluted sample of the nanocrystal in hexane was deposited on the TEM grid and dried in air.

The setup for the time-resolved fluorescence measurements in 900nm region consists with a time-correlated single photon counting setup utilizing SPC-630 single-photon counting PCI card (Becker & Hickle GmbH). A picosecond diode-laser was used as the photo-excitation source operated at 400 nm (Picoquant) along with an id50 avalanche photodiode (Quantique). The filtration of the signals was done by using 400nm, 532nm, 750nm and 900nm long-pass optical filters. Time – resolved PL measurements in 1300 nm region were obtained by Time-

Correlated Single Photon Counting (TCSPC) system based on InGaAs TE cooled single photon avalanche photodiode (ID Quantique) with a resolution of 200 picoseconds to obtain 10% quantum efficiency, SPC-130-EM Counting Module and BDL-488-SMN laser (Becker & Hickle) with pulse duration of 50 picoseconds and wavelength of 488 nm, CW power equivalent of about 0.5 mW, externally triggered at 1MHz repetition rate. Long-pass optical filters at 500 nm and 1300nm were used to exclude the laser line and the possible emission of CdS matrix of the detected emission signal.

2.4 Fluorescence quantum yield measurements.

A similar technique as described in Semonin *et al.,* [50] was used to obtain the absolute value of quantum yield measurements. The elimination of a reference and the ability of simultaneous measurement of the absorbance at the excitation wavelength with correction to reflectance and scattering losses using integrating sphere were advantageous in the project. A CW Laser Diode Module (wavelength of 808nm with power of 1 W modulated by optical chopper at 30Hz) was used as the excitation source and IS200-4, (Thorlabs) was applied for the spatial averaging the integrating sphere. This light was measured by broadband of 0.1-20 μm with a UM9B-BL-DA pyroelectric photo detector (Gentec-EO) and a lock-in amplifier SR 830 (Stanford Research) was used to modulate the signal from the detector. To set the light intensity to the optimum range of the detector and the lock-in amplifier, the signal receiving from the integrating sphere was attenuated with a neutral density filter. The energy yield obtained from the ratio between emitted and absorbed light was transformed to the quantum yield considering the difference in photon energies for the laser and the PL band (PL band was used average energy). And the final quantum yield value was corrected by transmission of applied edge pass filters.

CHAPTER 3: RESULTS AND DISCUSSION

The encapsulation of the near IR emitting PbS nanocrystals in to solid matrices was done using the recently reported SMENA method, [48] allowing these QDs to have gap-free fusion in to a wide band gap semiconductor host matrices. As the first step of the reported SMENA methodology, the nanocrystals were synthesized using the hot-injection method to grow monodisperse PbS nanocrystals, followed by the formation of a wide band gap semiconductor material via cation exchange. The formation of monodisperse QDs in endorsed by the use of non-coordinating solvents like ODE for the synthesis[47]. The lattice-matched hetero-interface between PbS and CdS creates a Type I band alignment as illustrated in Figure 3.1, providing localization of excited both electrons and holes in the core of the structure.

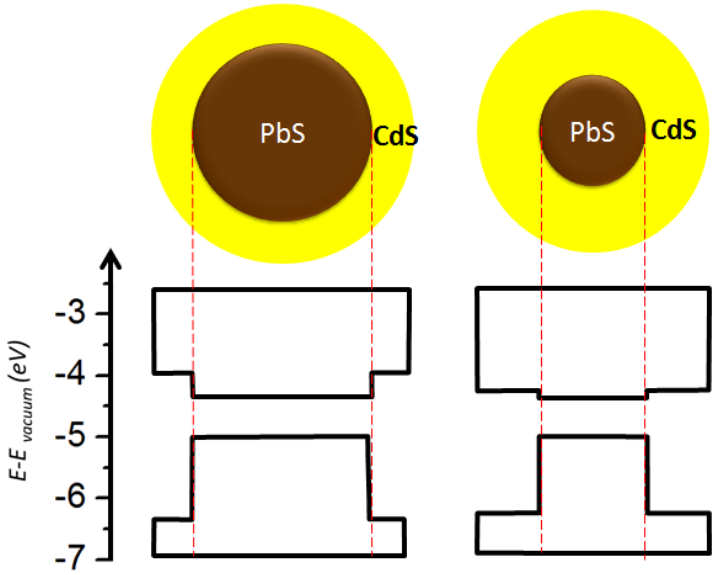

Figure 3.1 – Relative Type-I alignment of PbS/CdS core/shell structure with PbS diameter of 4 nm and 6 nm

As the second step, the semiconductor nanocrystal core/shells were spin coated on to a FTO glass substrate which after which the OA ligands were exchanged to thermally degradable

MPA ligands. The film was heated at 150 °C to promote the removal of the exchanged MPA and to allow the respective CdS domains to be fused well to perform the array of PbS/CdS core/shells. Then, the nanocrystal film was processed through the SILAR method[49] to fill the additional pores to neutralize the carrier trapping at the surfaces of the CdS matrix. This pore-filling method increases the stability of the PbS nanocrystal array increasing the average refractive index of the film (n).

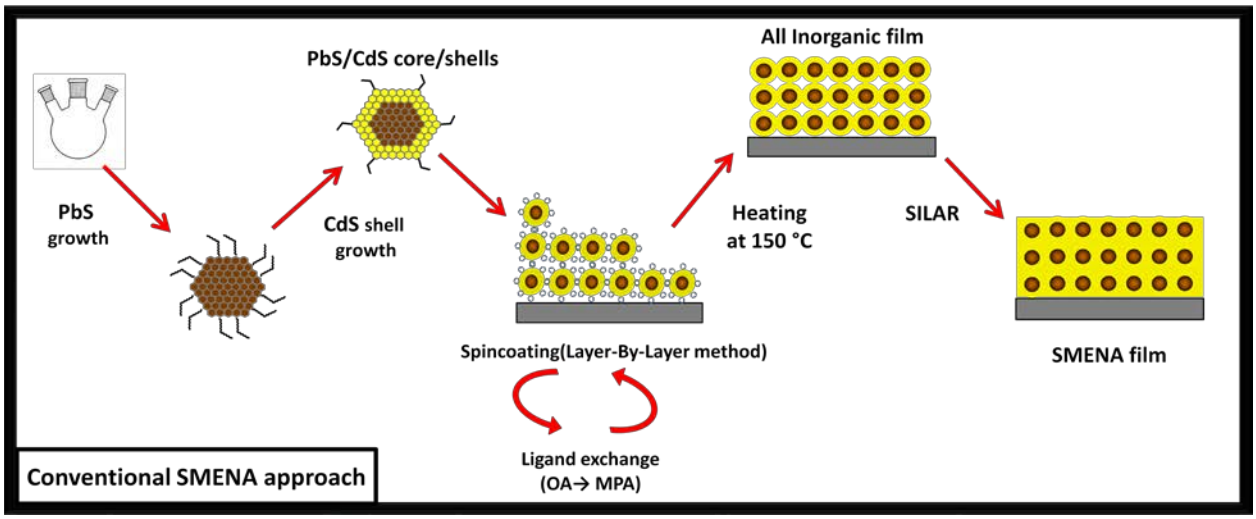

Figure 3.2 – Illustration of the key steps involving the conventional SMENA approach

In the modified SMENA approach (Figure 3.3), the colloidal state of the semiconductor nanocrystals used for the films contained a mixture of PbS/CdS core/shells with CdS seeds of 430 nm size. As explained in the experimental section, the ratios were calculated according to first exciton absorption peaks of the respective QDs.

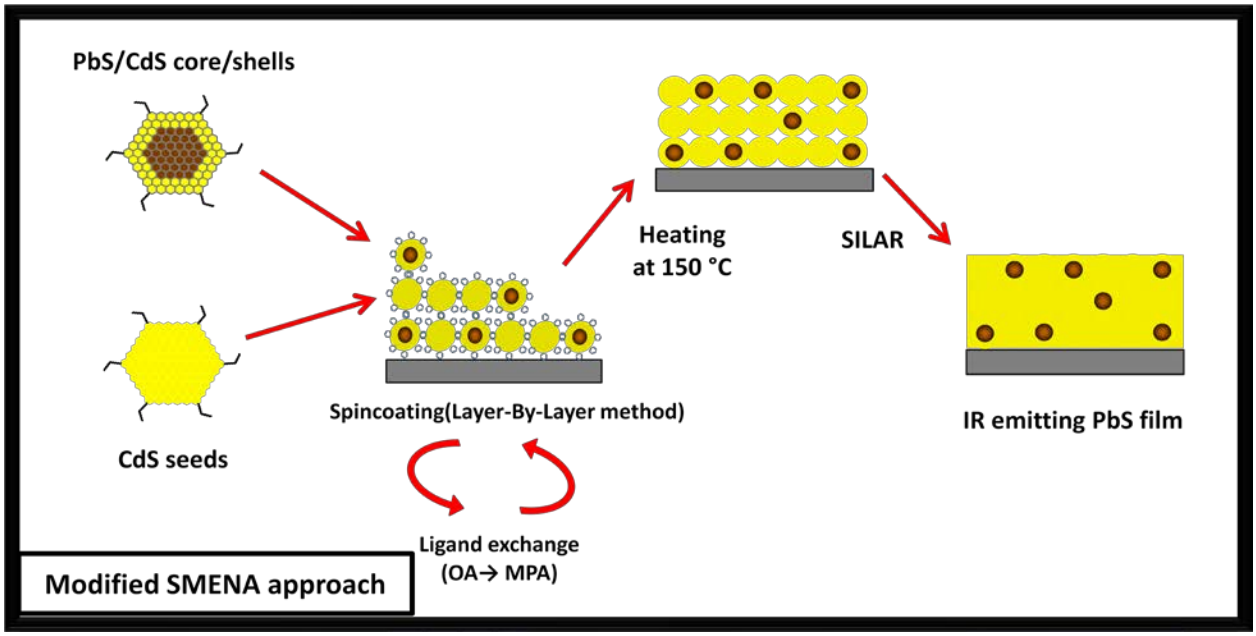

Figure 3.3 – Illustration of the key steps involving the modified SMENA approach (PbS/CdS is mixed with CdS seeds with similar diameter)

The key factor of enhancing the radiative recombination probability of a matrix encapsulated nanocrystal array is the confinement of the photo-induced charges. The work of Khon *et al.,* [31] report achieving a better localization of the excitons by increasing the thickness of the shell structure, ΔH, at the colloidal stage which determines the optimum value of the R_{edge} value ($R_{edge} = 2 \times \Delta H$) in a film. A larger R_{edge} leads to the better separation between embedded nanocrystals; providing a better suppression to the interparticle charge and energy transfer increasing the radiative recombination more probable. Also, the charge transfer rate between adjacent nanocrystals is dependent on the R_{edge} value or the shell thicknesses of nearby core/shell structures as illustrated in the Figure 3.4.

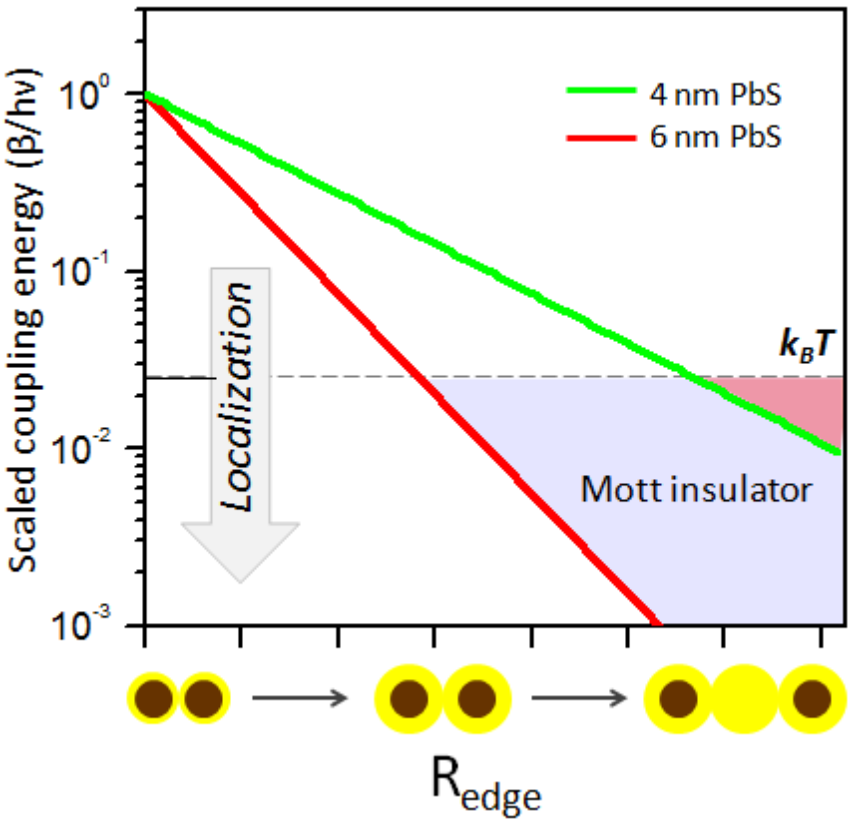

Figure 3.4 – WKB calculation of the coupling energy (β) dependence on the interparticle distance (R_{edge}) in relative units of scale. The colored areas indicate the regime of strongly localized charges

It is assumed that the rate of the charge tunneling between them is identified as a single exponential dependant function of the width of the potential barrier separating the neighboring nanocrystals. By the use of Wentzel-Kramer-Brillouin (WKB) approximation, this tunneling rate can be simplified to $\Gamma \sim \exp\left(-2(2m\Delta E/\hbar^2)^{1/2}R_{edge}\right)$ [31]. Here the potential barrier height between electron and hole state in nearby nanocrystals is denoted by ΔE. The regime of strong localization of charges is obtained when the coupling energy of these nanocrystals ($\beta = \hbar\omega\Gamma$) becomes lower than the thermal energy (kT), which is also known as the Mott Insulator Transition (MIT). Since the localization of the photo-induced charges in the Type I aligned

core/shells are more prominent in larger QDs (Figure 3.1), the R_{edge} distance which this MIT occurs gets shortened with the increase of the diameter of the QD. This is significantly observed by the comparison of coupling energies of adjacent dots for the case of PbS QDs of 4 nm and 6nm in diameter encapsulated in to CdS matrix by SMENA procedure. According the Figure 3.4, it is clear that the R_{edge} value associated with the MIT in 6 nm PbS/CdS solids is about 2 times less than the value of 6 nm PbS/CdS solid. The figure preserves the correct lengths ratio corresponding to MIT transitions between different dot diameters.

Due to the small potential barrier that electrons are facing in PbS QDs with a small diameter, it is necessary to have a thick shell of CdS to achieve a strong localization of the excited charges. But the practical growth of a thick shell of CdS can lead to a higher interfacial strain of the lattice structure increasing the probability of the formation of defect structures. These defects can create additional non-radiative decaying of the generated excitons, lowering the performance of the films.[51-53]

As an alternative solution to this challenge, the R_{edge} value of these nanocrystals can be increased by introducing CdS QDs of the same size, replacing a part of the PbS/CdS core/shell structure as described in modified SMENA method (Figure 3.3). This method would allow a greater interparticle separation without any additional shell growth on the PbS QDs providing a strong localization of the charges. On top of the greater performance, this method provides a better mode of controlling the balance between the packing density (filling factor) of the IR QDs and the emission quantum yield by changing the ratio of used PbS/CdS to CdS seeds at their colloidal stage. For instance, using a low density of the PbS nanocrystals in the solid matrix results a enhancement of the recombination of the photo-excited charges due the low rate of

tunneling between adjacent QDs. Even with a relatively low packing density, this would result a greater emission quantum yield of the solid matrix. Conversely, increasing the filling factor of the PbS nanocrystals in the matrix would result a reduction of the average separation (low R_{edge} distance) between the PbS domains. But due to the high rate of tunneling (incomplete localization) of the excited carriers present a significant drop of the fluorescence quantum yield.

To investigate the dependence of the photo-excited emission of the IR emitting PbS QDs on the interparticle separation, two separate sets of PbS embedded nanocrystal solids were fabricated using the aforementioned two techniques. In the first set, the R_{edge} distance was controlled using the conventional SMENA technique by varying the thickness of the synthesized PbS/CdS core/shells. In the second set, to control the R_{edge} distance, the modified SMENA technique was used by embedding the core/shells with a tunable fraction of CdS QDs of the same size. The synthesis of the PbS/CdS core/shells was performed using the cation exchange method[35] since this method provides an accurate control over the growth of the CdS shell which determines the optimum value of R_{edge} in both film architectures. A uniform formation of CdS shell on PbS core of a PbS with a diameter of 2.7 nm core surrounding a 1.3 nm CdS shell is illustrated in Figure 3.5 obtained from high resolution TEM image.

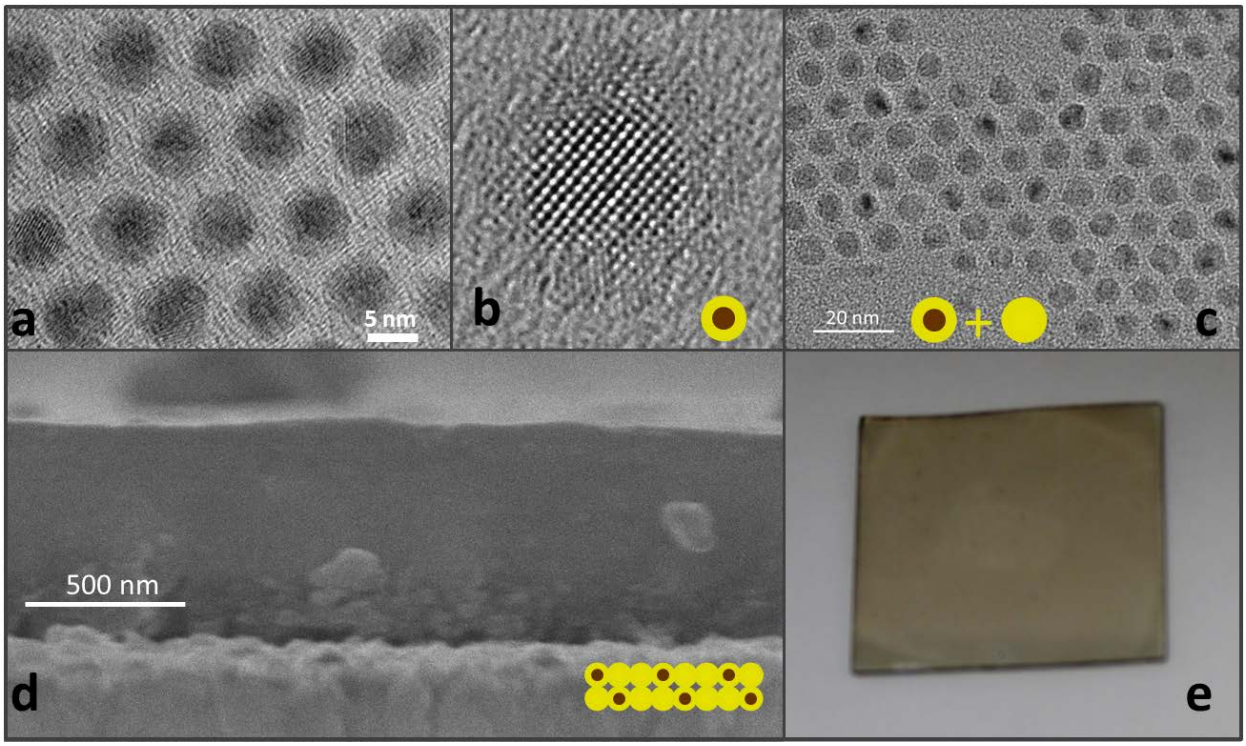

Figure 3.5 - (a), (b). High resolution TEM images of 2.7-nm PbS nanocrystals coated with a 1.3-nm CdS shell. (c). The mixture of PbS/CdS nanocrystals and 5.0-nm CdS nanocrystals prior to the deposition on a glass substrate. Scanning electron microscope (SEM) (d) and photo (e) images of a CdS-encapsulated PbS nanocrystal film.

When analyzing the time-resolved spectroscopic measurements of the near-IR emitting PbS nanocrystals in the solid matrices, the films fabricated using the conventional SMENA method showed an increase in the fluorescence decay with the increase of the R_{edge} value. This is aligning well with the predictions, that the transfer of charges via non-radiative decaying gets a lower fraction of the excited charges in larger R_{edge} values. In principle, charge trapping on surfaces of the unpassivated CdS matrix can shorten the decay of excitons in PbS solids;

however, the rate of this process is slower than the rate of charge and energy transfer within the solid matrices.[54]

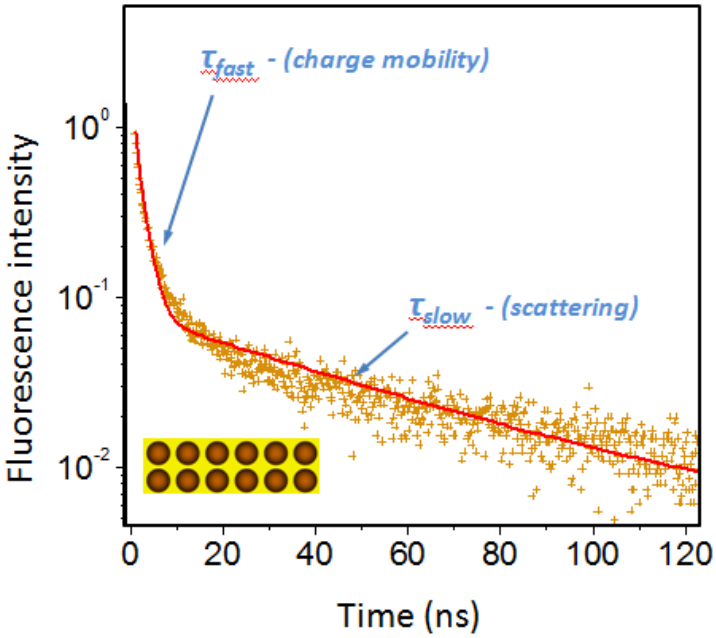

Figure 3.6 – Fluorescence lifetime of PbS in CdS matrix using conventional SMENA method

As illustrated in Figure 3.6, the fast component of the fluorescence lifetime decay represents the mobilization of the charges between the nanocrystals in the film and the slow component represents the trapping of the charges in the unpassivated CdS matrices.

As mentioned before, the rate of tunneling between resonant states diminish exponentially with R_{edge}, while the rate of energy transfer diminishes with a dependence of R_{edge}^{6} with the non-radiative dipole-dipole coupling approximation (Förster Resonance Energy Transfer).[55] The comparison experiment of the effect of the charge and the energy transfer to the fluorescence decay if illustrated from the Figure 3.7(b). The fast component (τ_{fast}) of the each decay rate for different R_{edge} values in the Figure 3.7(a) was plotted with the WKB ($\sim e^{\alpha Redge}$) and FRET ($\sim R_{edge}^{6}$). From the curve, it is evident that the fast component of the fluorescence decay rate

corresponds mainly due to the interparticle charge transfer process with a single exponential decay and not to the energy transfer. This is an important finding that the primary mechanism that involved with the formation of the dark states by exciton dissociation is due to the charge transfer through the nanocrystals in the solid matrix.

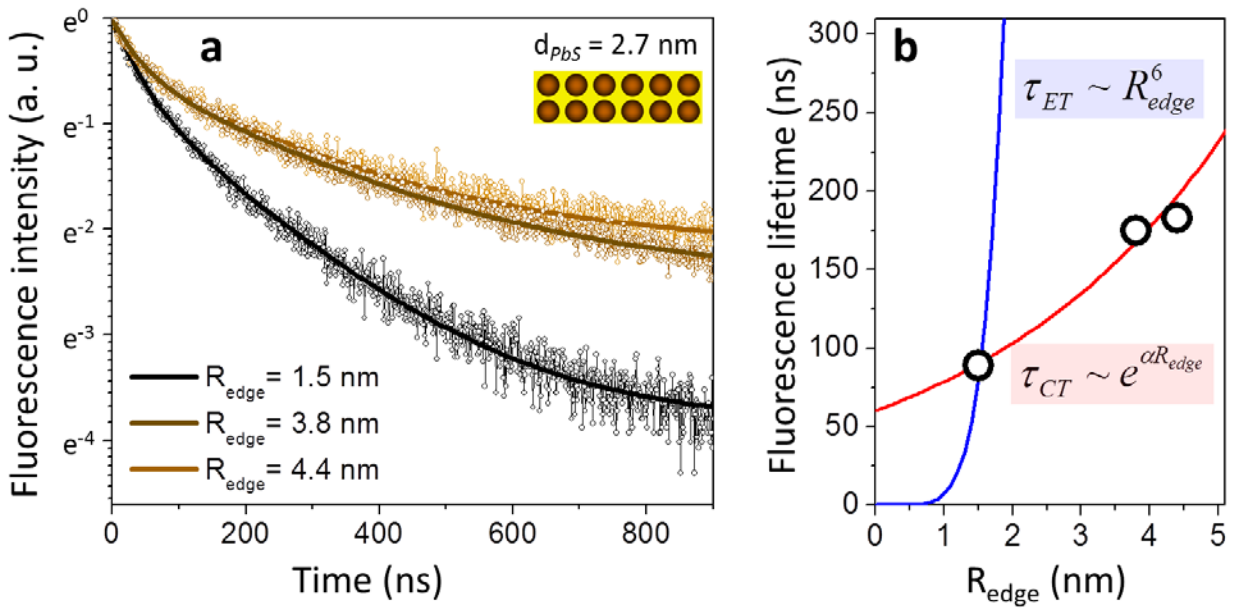

Figure 3.7- (a) Fluorescence intensity decay of conventional SMENA films representing different R_{edge} values. (b) The comparison of predicted (WKB approximation using a single fitting parameter - C) and measured exciton lifetimes for CdS-encapsulated PbS nanocrystals.

The measured fluorescence lifetime value of matrix-encapsulated films using the conventional SMENA technique acquired a maximum value of 190 nanoseconds with a R_{edge} value 4.4 nm. It is significant that this saturated limit of the lifetime if far less than the value of the same PbS/CdS core/shell structure in its colloidal state which is 2.8 microseconds which is illustrated in the Figure 3.8.

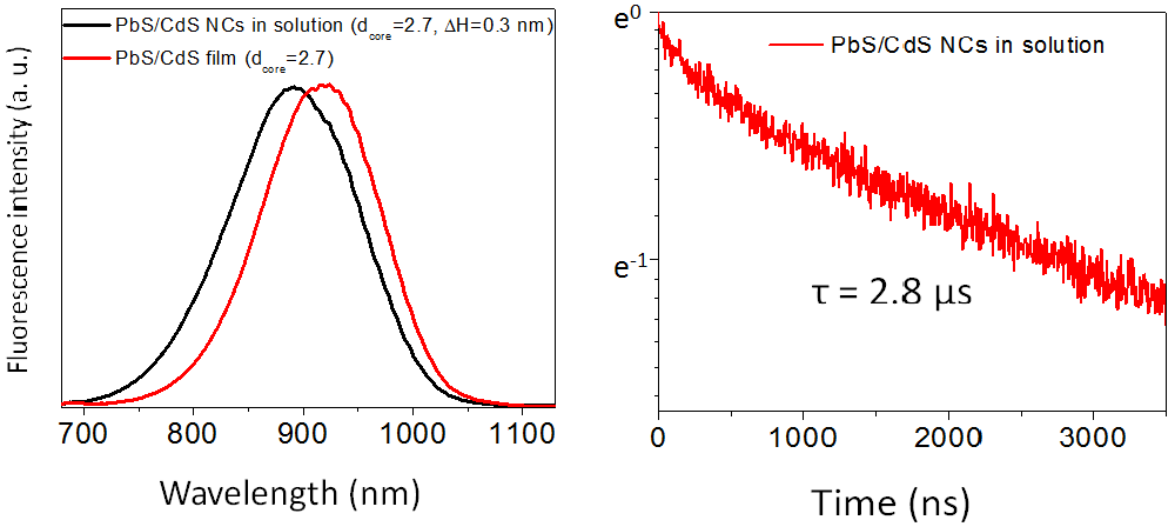

Figure 3.8 – Fluorescence intensity comparison of the PbS/CdS core/shell at colloidal state.

Beyond this saturation limit, the further increase of the CdS shell thickness fails to enhance the lifetime even in the solution state, since the trap state emission becomes more dominant process in the charge carrier dissociation. With further growth of 3-4 monolayers results a high strain at the hetero-interface, increasing the trap state emission compared to the band gap emission.[47]

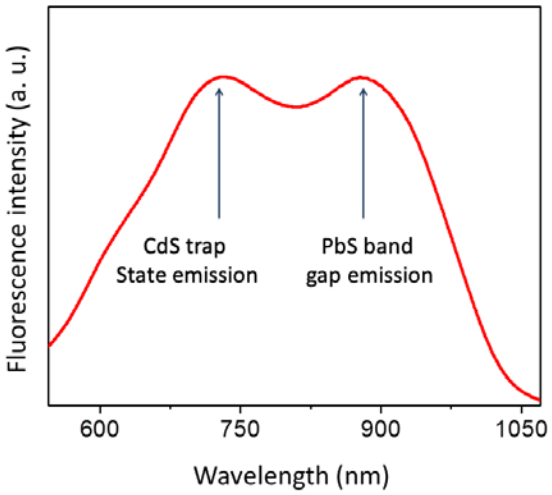

Figure 3.9 - CdS trap state emission affecting the PbS band gap emission

On the other hand, the modified SMENA technique provides a better method of increasing the R_{edge} value in films despite of growing additional monolayers of CdS shell around the PbS

nanocrystals. This allows a better suppression of the escaping of the photo-induced charges without any additional strain in the solid matrices preventing any rate-limiting defects.

To investigate the characteristics of the proposed method, several films were fabricated varying the fraction of the CdS seeds to PbS/CdS core/shells as an increasing order. All the calculations related to the ratios were done by considering the absorbance peak of the samples used. In principal, when integrating additional CdS domains in the core/shell structure in a film, the average particle distance become more than twice the value of the thickness of the shell

The relationship between the molar concentrations of the both types of nanoparticles and the partial number density of the particles in the mixture was analyzed using the TEM images. From the Figure 3.10, the ratio of the PbS/CdS to CdS nanoparticles can be easily identified by the corresponding population of each dot in the TEM image.

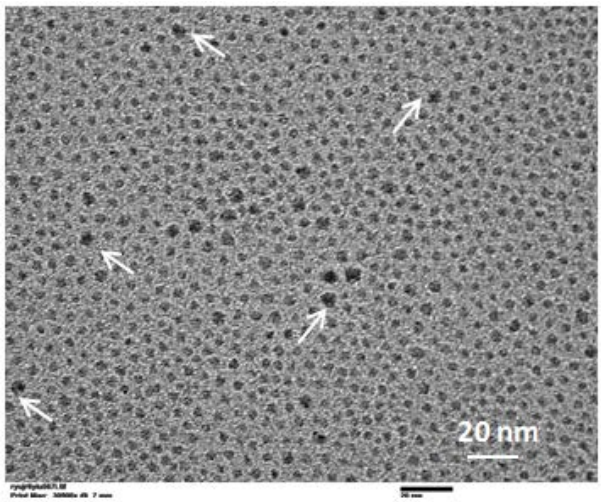

Figure 3.10 - A characteristic TEM image of 4.3-nm CdS and 6.0-nm PbS/CdS nanocrystal mixture. Arrows mark the location of PbS/CdS core/shell structures

From the TEM image, it is clearly identified the core/shell nanocrystals with a larger radii and a darker shading marked by white arrows. The image corresponds to 5.2 nm PbS/CdS

core/shell structure and 4.3 nm sized CdS seeds. Since the initial concentration of the solutions used were known, the number density of each nanoparticle can be estimated using this method. The ratio of the CdS to PbS/CdS dots in the film is used to PbS volume fraction, v_{PbS}, using the following equation.

Suppose that on average a unit length of the mixed nanocrystal film contains Nc of CdS and Np and core/shell nanocrystals. A unit volume of such film be given by $(N_P D_{P/C} + N_C D_C)^3$, where Dp/c and Dc are the average diameters of PbS/CdS and CdS NCs, respectively. The number of PbS cores in a unit volume will be given by $N_p / N \times (N_P + N_C)^3$, where $N = N_P + N_C$, where N = Nc + Np. Therefore the volume fraction can be expressed as:

$$\frac{V_{PbS}}{V_{CdS}} = \frac{N_P / N \times (N_P + N_C)^3 \times 4/3\,\pi R_{core}^3}{(N_P D_{P/C} + N_C D_C)^3} = \frac{(n+1)^2 \times 4/3\,\pi R_{core}^3}{(nD_C + D_{P/C})^3}$$

Here, the value $n=N_{PbS}/N_{CdS}$, and R_{core} is the average radius of the PbS core in PbS/CdS core/shell NCs.

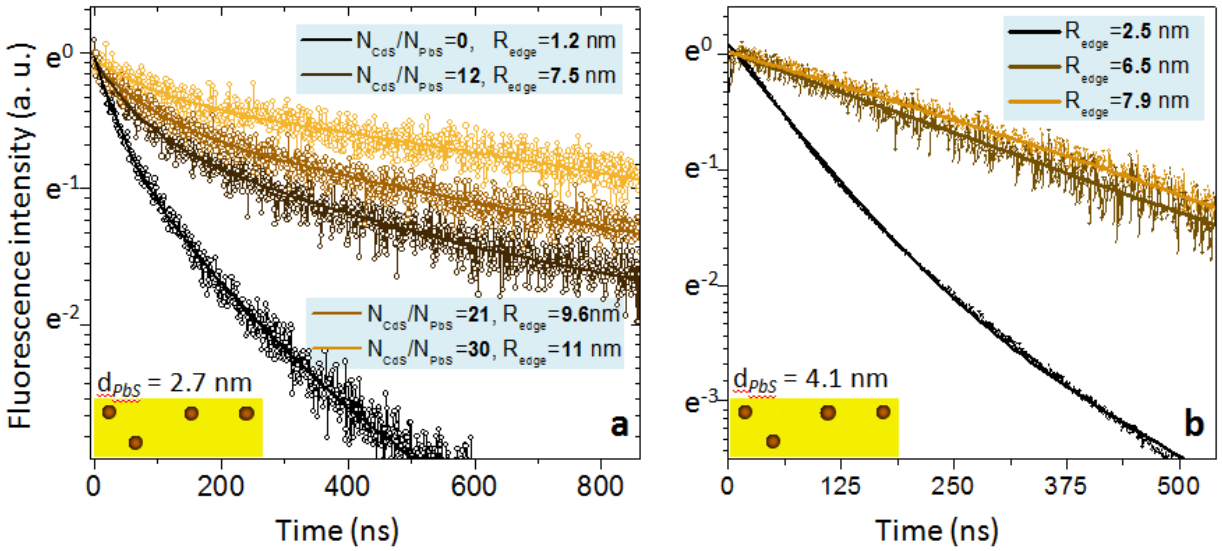

Figure 3.11 - Fluorescence intensity decay of near-IR emitting PbS NCs (a) d=2.7 nm and (b) d=4.1 nm encapsulated into CdS matrices as a function of increasing N_{PbS}/N_{CdS}.

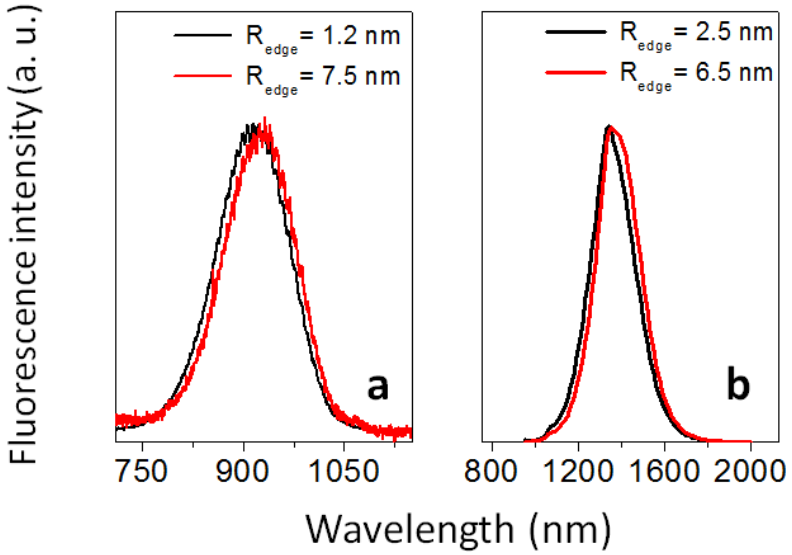

Figure 3.12 – Steady-state emission of modified SMENA films (a) d_{PbS} = 2.7 nm with N_{CdS}/N_{PbS}=0 (black) and N_{CdS}/N_{PbS}=4 (red) and (b) d_{PbS} = 4.1 nm with N_{CdS}/N_{PbS}=0 (black) and N_{CdS}/N_{PbS}=4 (red).

Figure 3.11shows that with the increase in R_{edge} value by the mixture of CdS (d_{CdS} = 4.3 nm) and PbS/CdS (d_{PbS} = 2.7 nm), increases of fluorescence lifetime decay as expected from the WKB approximation. The fastest decay process in Figure 3.11with a R_{edge} of 1.2 nm corresponds to film fabricated without any CdS nanocrystals in between PbS domains, which is similar to the films fabricated by conventional SMENA technique. Compared to the other films, the thin CdS shell (ΔH~ 1 nm) in this film, enable only a partial localization of the photo-induced charges leading to a lifetime of 95 ns. Increase of the CdS ration to the PbS used in the film leads to the increase of interparticle distance, R_{edge}, from a value of 1.2 nm to 11 nm providing a maximum separation of the nanoparticles than of the conventional approach. With the maximum value of the R_{edge} value, a fluorescence decay time of 0.98 microseconds was observed, which is four times greater value of the best performing nanocrystal solid fabricated using the conventional SMENA method. Likewise, the observed exciton lifetime was found to be longer than that of previously reported PbS film architectures utilizing hybrid molecular ligands.[35] This phenomenon can tentatively attributed to a suppressed non-radiative decay in CdS-encapsulated nanocrystals. However, the fluorescence lifetime of larger PbS nanoparticles ($\lambda \approx 1300$ nm) was observed to be shorter than that of the smaller PbS QDs. As shown in Figure 3.11(b), the longest report lifetime is τ = 480 ns which could be explained by the difference in the radiative decay of PbS nanoparticle according to the diameter. Also, red shift of ~20 nm of the fluorescence peak can be observed when increasing the N_{CdS}/N_{PbS} which could be mainly due the delocalization of the electronic wave function in to the CdS matrix.

The fabricated films provide a better structure for the assembly of the PbS nanoparticles. However, the structure still contains interparticle gaps between the nanocrystal solids. To reduce the density of these gaps and fuse the core/shell structures, additional CdS were partially filled

using the SILAR method. It is reported that such treatment increases the refractive index reducing the density of dangling bonds. [31] According to the Figure 3.13, the application of 6 SILAR cycles to a film with R_{edge} of 1.5 nm, results a 55% increase of the fluorescence lifetime in the modified SMENA film. Numerically, the slower component of the fluorescence intensity decay has increase from a value of 90 ns to 150 ns which significantly express the reduction of charge trapping in the film.

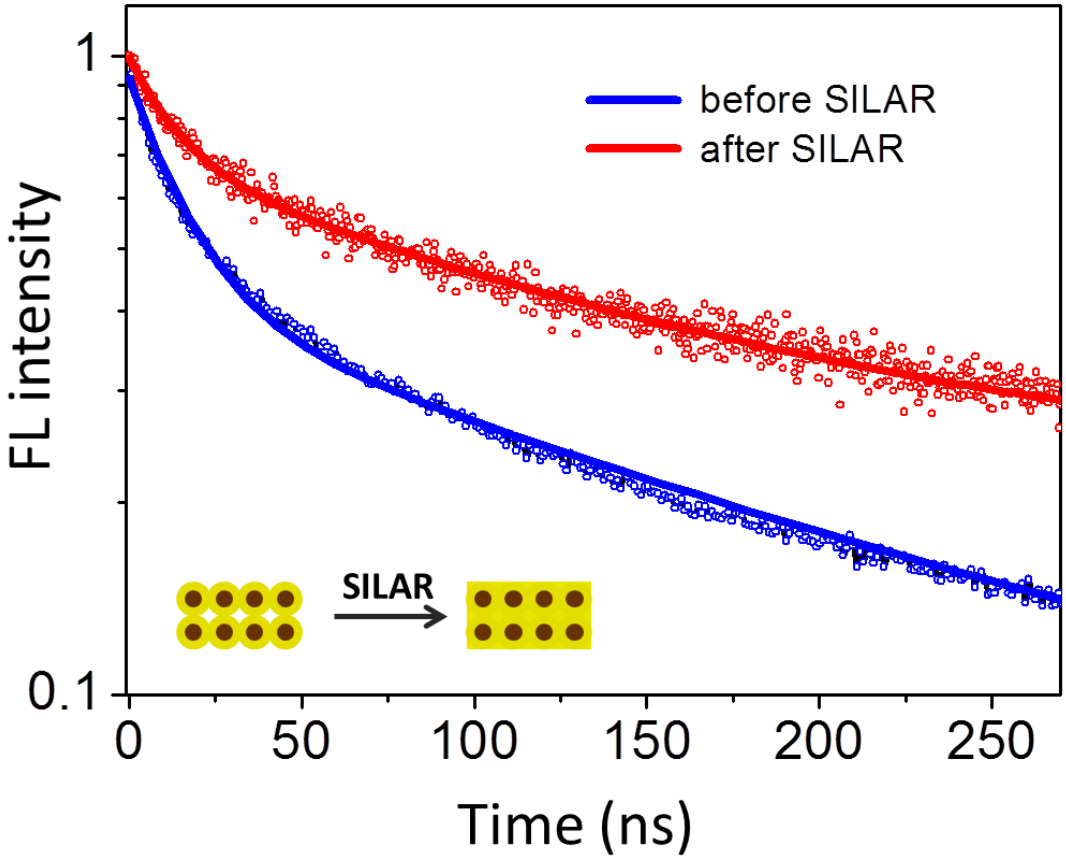

Figure 3.13 - Suppression of the charge trapping on the surface of modified PbS/CdS SMENA film by additional SILAR passivation.

Temperature dependence of the fabricated films is crucial fact when considering the performance when they are implemented on light emitting devices. In the present approach, the modified SMENA films shows and excellent resistivity to thermal degrading at lower temperatures as the hetero-epitaxial bonding of the PbS nanoparticle surfaces prevents low-temperature oxidation processes. The thermal degradation is observed only at higher temperature via phase transition of the lattice structures.

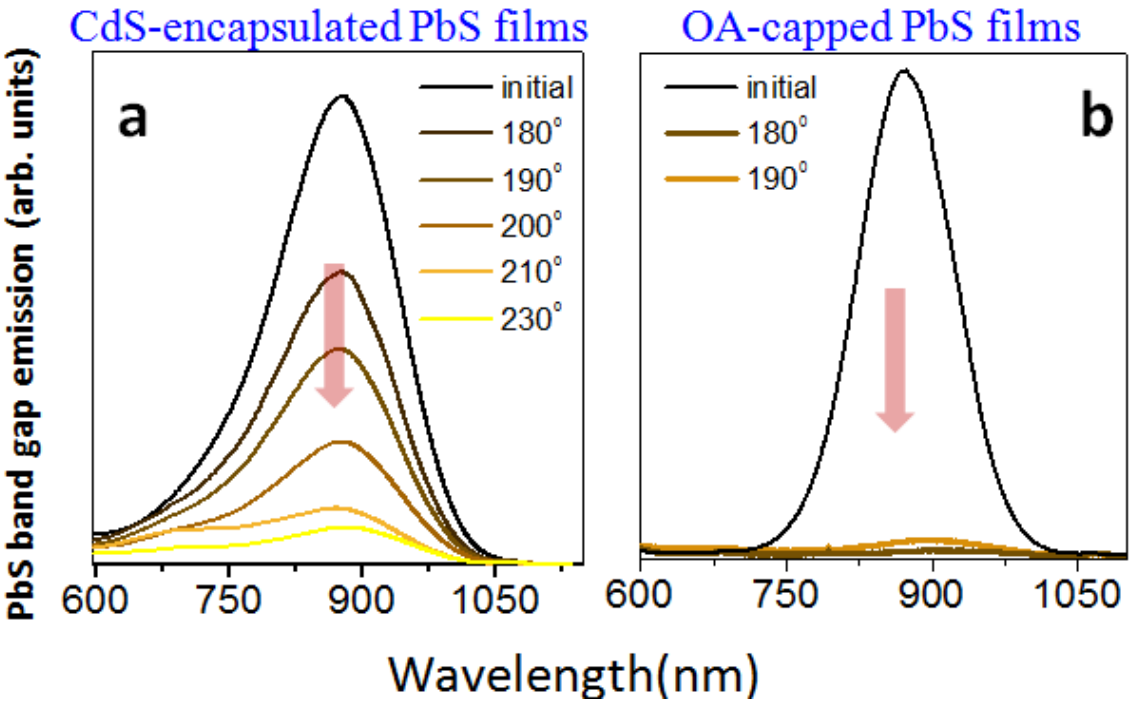

Figure 3.14 - Comparison of the thermal stability of (c) OA-capped and (b) CdS encapsulated PbS nanocrystal arrays.

Here, the temperature dependency of the fabricated films was tested with comparison to the oleic acid (OA)-capped PbS nanocrystal films. Both types of films were subjected to heating in air while changing the temperature and the intensity of the band gap emission was measured at each temperature. Figure 3.14 shows the emission spectra of films versus the substrate temperature fabricated by (a) modified SMENA technique and (b) (OA)-passivated PbS

nanocrystal films with an R_{edge} of 2.8 nm. It can be clearly seen that the band gap emission of both films results in a gradual drop which was identified as the sintering temperature of the PbS nanocrystal solids. The modified SMENA films shows an excellent thermal stability showing a better emission at higher temperatures as high as T ≈ 200 °C, compared to the OA-capped PbS nanocrystal solids which that value lies 90-100 °C below. The oxidation in the solid matrix surface is partially responsible for degradation of the emission in SMENA films which can be clearly identified by the Figure 3.15.

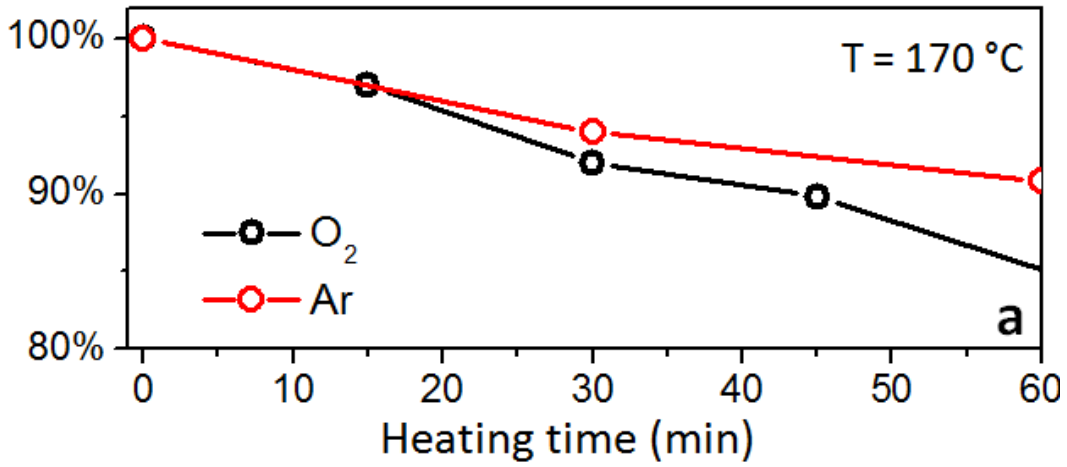

Figure 3.15 - Time dependence of relative band-edge emission peak area for CdS-encapsulated PbS nanocrystal arrays at 170 ^{o}C (R_{egde} ≈ 2.8 nm).

The figure shows the time dependency of modified SMENA films, exposed to heat at 170 °C for a longer time period in air and in an inert condition. A slightly faster decay of the curve in air compared to the film heated in inert environment suggests that oxidation is partly responsible for the loss of emission at elevated temperatures.

When considering the performance of the IR emission of the modified SMENA films, the emission quantum yield was calculated for the films containing PbS QDs with larger diameter

($\lambda_{FL} \approx 1300$ nm). The methodology used is adapted from Semonin *et al.*,[50] which was designed to eliminate the use of a reference dye and to provide the possibility for simultaneous measurement at excitation wavelength of absorbance. The emission quantum yield values of for different R_{edge} value is as illustrated below. The relative error of Quantum Yield measurement is about 15%. The effects of self-absorption were neglected due to low optical density of the samples.

Sample (λ_{PbS}=1300 nm)	PbS volume fraction (ν_{PbS})	Optical density @808 nm	Quantum Yield, %	Life time, ns
R_{edge}=2.5 nm	0.24	0.032	2.0	105
R_{edge}=6.5 nm	0.096	0.015	3.3	350
R_{edge}=7.9 nm	0.07	0.015	3.7	480

Table 3.1- Quantum yield of CdS-encapsulated PbS nanocrystal solids emitting at λ_{PbS} = 1300 nm.

From the measurements, it can be clearly seen that the maximum value obtained for the emission quantum yield is 3.7 % in the solid matrix of 7.9 nm R_{edge} value. This emission quantum yield can be identified as the largest reported value for IR emitting nanocrystal solid film. The considerable difference in the quantum yield measurements in the solid form and its colloidal state is attributed to the charge dissociation pathways when transferring the PbS nanocrystals from solution to its solid form. Even with this value, it is evident that the proposed method provides a better alternative in fabricating IR emitting PbS nanocrystal films which can be engineered in the device fabrication in the future.

CHAPTER 4: CONCLUSION

The reported strategy exhibits a better alternative in fabricating IR emitting PbS nanocrystal solids. The encapsulation of the PbS QDs in to all inorganic matrices of CdS provides a better passivation at the nanocrystal surfaces providing a better quantum confinement. The stable host matrices enable the suppression of non-radiative charge dissociation through surface trap states and inter-particle charge and energy transfer processes. Through this modified SMENA technique a significant increase in fluorescence lifetime was achieved with a highest value of 0.98μs for PbS QDs with a diameter of 2.7 nm which is four times greater the value obtained from the conventional SMENA technique. The well fused lattice structure provides a high emission quantum yield of 3.7% which is a significant value considering the solid state IR emission of the previously reported thin film devices. In addition to the higher quantum yield, these films show an excellent thermal stability, which is a promising fact when engineering them in to solid state IR emitting technologies.

REFERENCES

[1] Khon, E.; Hewa-Kasakarage, N.; Nemitz, I.; Acharya, K.; Zamkov, M. Tuning the Morphology of Au/CdS Nanocomposites through Temperature-Controlled Reduction of Gold-Oleate Complexes. *Chem. Mater.* **2010**, *22*, 5929-5936.

[2] Caruge, J. M.; Halpert, J. E.; Wood, V.; Bulovic, V.; Bawendi, M. G. Colloidal quantum-dot light-emitting diodes with metal-oxide charge transport layers. *Nature Photonics* **2008**, *2*, 247-250.

[3] Coe, S.; Woo, W.; Bawendi, M.; Bulovic, V. Electroluminescence from single monolayers of nanocrystals in molecular organic devices. *Nature* **2002**, *420*, 800-803.

[4] Colvin, V. L. *Nature* **1994**, *370*, 354.

[5] Mattoussi, H.; Radzilowski, L. H.; Dabbousi, B. O.; Thomas, E. L.; Bawendi, M. G.; Rubner, M. F. Electroluminescence from heterostructures of poly(phenylene vinylene) and inorganic CdSe.. *J. Appl. Phys.* **1998**, *83*, 7965.

[6] Rogach, A.; Gaponik, N.; Lupton, J.; Bertoni, C.; Gallardo, D.; Dunn, S.; Li?Pira, N.; Paderi, M.; Repetto, P.; Romanov, S.; O'Dwyer, C.; Sotomayor?Torres, C.; Eychmüller, A. Light-Emitting Diodes with Semiconductor Nanocrystals. *Angewandte Chemie International Edition* **2008**, *47*, 6538-6549.

[7] Schlamp, M. C. *J. Appl. Phys.* **1997**, *82*, 5837.

[8] Sun, Q.; Wang, Y. A.; Lin, S. L.; Wang, D.; Zhu, T.; Xu, J.; Yang, C.; Li, Y. Bright, multicoloured light-emitting diodes based on quantum dots. *Nature Photonics* **2007**, *1*, 717-722.

[9] Tessler, N.; Medvedev, V.; Kazes, M.; Kan, S.; Banin, U. Efficient Near-Infrared Polymer Nanocrystal Light-Emitting Diodes. *Science* **2002**, *295*, 1506-1508.

[10] Fafard, S.; Hinzer, K.; Raymond, S.; Dion, M.; McCaffrey, J.; Feng, Y.; Charbonneau, S. Red-Emitting Semiconductor Quantum Dot Lasers. *Science* **1996**, *274*, 1350-1353.

[11] Klimov, V. I.; Mikhailovsky, A. A.; Xu, S.; Malko, A.; Hollingsworth, J. A.; Leatherdale, C. A.; Eisler, H.; Bawendi, M. G. Optical gain and stimulated emission in nanocrystal quantum dots. *Science* **2000**, *290*, 314-317.

[12] Klimov, V. I.; Ivanov, S. A.; Nanda, J.; Achermann, M.; Bezel, I.; McGuire, J. A.; Piryatinski, A. Single-exciton optical gain in semiconductor nanocrystals. *Nature* **2007**, *447*, 441-446.

[13] Hillhouse, H. W.; Beard, M. C. Solar cells from colloidal nanocrystals: Fundamentals, materials, devices, and economics. *Current Opinion in Colloid & Interface Science* **2009**, *14*, 245-259.

[14] Huynh, W. U.; Dittmer, J. J.; Alivisatos, A. P. Hybrid nanorod-polymer solar cells. *Science* **2002**, *295*, 2425-2427.

[15] McDonald, S. A.; Konstantatos, G.; Zhang, S.; Cyr, P. W.; Klem, E. J. D.; Levina, L.; Sargent, E. H. Solution-processed PbS quantum dot infrared photodetectors and photovoltaics. *Nature Materials* **2005**, *4*, 138-142.

[16] Gur, I. Air-Stable All-Inorganic Nanocrystal Solar Cells Processed from Solution. *Science* **2005**, *310*, 462; 462-465; 465.

[17] Guo, Q.; Kim, S. J.; Kar, M.; Shafarman, W. N.; Birkmire, R. W.; Stach, E. A.; Agrawal, R.; Hillhouse, H. W. Development of CuInSe2 Nanocrystal and Nanoring Inks for Low-Cost Solar Cells. *Nano Lett.* **2008**, *8*, 2982-2987.

[18] Maria, A.; Cyr, P. W.; Klem, E. J. D.; Levina, L.; Sargent, E. H. Solution-processed infrared photovoltaic devices with >10% monochromatic internal quantum efficiency. *Appl. Phys. Lett.* **2005***, 87*, 213112.

[19] Leschkies, K. S.; Beatty, T. J.; Kang, M. S.; Norris, D. J.; Aydil, E. S. Solar Cells Based on Junctions between Colloidal PbSe Nanocrystals and Thin ZnO Films. *ACS Nano* **2009***, 3*, 3638-3648.

[20] Wang, R. Y.; Feser, J. P.; Lee, J.; Talapin, D. V.; Segalman, R.; Majumdar, A. Enhanced Thermopower in PbSe Nanocrystal Quantum Dot Superlattices. *Nano Lett.* **2008***, 8*, 2283-2288.

[21] Schneider, J. J.; Hoffmann, R. C.; Engstler, J. ö.; Soffke, O.; Jaegermann, W.; Issanin, A.; Klyszcz, A. A Printed and Flexible Field-Effect Transistor Device with Nanoscale Zinc Oxide as Active Semiconductor Material. *Adv Mater* **2008***, 20*, 3383-3387.

[22] Lee, S.; Jeong, S.; Kim, D.; Park, B. K.; Moon, J. Fabrication of a solution-processed thin-film transistor using zinc oxide nanoparticles and zinc acetate. *Superlattices and Microstructures* **2007***, 42*, 361-368.

[23] Ridley, B. A.; Nivi, B.; Jacobson, J. M. All-Inorganic Field Effect Transistors Fabricated by Printing. *Science* **1999***, 286*, 746-749.

[24] Talapin, D. V. PbSe Nanocrystal Solids for n- and p-Channel Thin Film Field-Effect Transistors. *Science* **2005***, 310*, 86; 86-89; 89.

[25] Reiss, P.; Protière, M.; Li, L. Core/Shell Semiconductor Nanocrystals. *Small* **2009***, 5*, 154-168.

[26] Pietryga, J. M.; Werder, D. J.; Williams, D. J.; Casson, J. L.; Schaller, R. D.; Klimov, V. I.; Hollingsworth, J. A. Utilizing the lability of lead selenide to produce heterostructured nanocrystals with bright, stable infrared emission. *J. Am. Chem. Soc.* **2008***, 130*, 4879-4885.

[27] Bowers, M. J.; McBride, J. R.; Rosenthal, S. J. White-Light Emission from Magic-Sized Cadmium Selenide Nanocrystals. *J. Am. Chem. Soc.* **2005***, 127*, 15378-15379.

[28] Li, H.; Brescia, R.; Krahne, R.; Bertoni, G.; Alcocer, M. J. P.; Dâ€™Andrea, C.; Scotognella, F.; Tassone, F.; Zanella, M.; De Giorgi, M.; Manna, L. Blue-UV-Emitting ZnSe(Dot)/ZnS(Rod) Core/Shell Nanocrystals Prepared from CdSe/CdS Nanocrystals by Sequential Cation Exchange. *ACS Nano* **2012***, 6*, 1637-1647.

[29] Dabbousi, B. O.; Rodriguez-Viejo, J.; Mikulec, F. V.; Heine, J. R.; Mattoussi, H.; Ober, R.; Jensen, K. F.; Bawendi, M. G. (CdSe)ZnS Core-Shell Quantum Dots: Synthesis and Characterization of a Size Series of Highly Luminescent Nanocrystallites. *J Phys Chem B* **1997***, 101*, 9463-9475.

[30] Lim, J.; Jun, S.; Jang, E.; Baik, H.; Kim, H.; Cho, J. Preparation of Highly Luminescent Nanocrystals and Their Application to Light-Emitting Diodes. *Adv Mater* **2007***, 19*, 1927-1932.

[31] Khon, E.; Lambright, S.; Khon, D.; Smith, B.; O'Connor, T.; Moroz, P.; Imboden, M.; Diederich, G.; Perez-Bolivar, C.; Anzenbacher, P.; Zamkov, M. Inorganic Solids of CdSe Nanocrystals Exhibiting High Emission Quantum Yield. *Advanced Functional Materials* **2012***, 22*, 3714-3722.

[32] van Veggel, Frank C. J. M. Near-Infrared Quantum Dots and Their Delicate Synthesis, Challenging Characterization, and Exciting Potential Applications. *Chem. Mater.* **2014***, 26*, 111-122.

[33] Chen, C.; He, X.; Gao, L.; Ma, N. Cation Exchange-Based Facile Aqueous Synthesis of Small, Stable, and Nontoxic Near-Infrared Ag2Te/ZnS Core/Shell Quantum Dots Emitting in the Second Biological Window. *ACS Appl. Mater. Interfaces* **2013***, 5*, 1149-1155.

[34] Zhu, C.; Jiang, P.; Zhang, Z.; Zhu, D.; Tian, Z.; Pang, D. Ag2Se Quantum Dots with Tunable Emission in the Second Near-Infrared Window. *ACS Appl. Mater. Interfaces* **2013***, 5*, 1186-1189.

[35] Kovalenko, M. V.; Schaller, R. D.; Jarzab, D.; Loi, M. A.; Talapin, D. V. Inorganically Functionalized PbS−CdS Colloidal Nanocrystals: Integration into Amorphous Chalcogenide Glass and Luminescent Properties. *J. Am. Chem.Soc.* **2012**, *134*, 2457−2460.

[36] Zhao, H.; Chaker, M.; Wu, N.; Ma, D. Towards Controlled Synthesis and Better Understanding of Highly Luminescent PbS/CdS Core/Shell Quantum Dots *J. Mater. Chem.* **2011**, 21, 8898- 8904.

[37] Wise, F. W. Lead Salt Quantum Dots: the Limit of Strong Quantum Confinement. *Acc. Chem. Res.* **2000***, 33*, 773-780.

[38] Friend, R. H.; Gymer, R. W.; Holmes, A. B.; Burroughes, J. H.; Marks, R. N.; Taliani, C.; Bradley, D. D. C.; Dos Santos, D. A.; Bredas, J. L.; Logdlund, M.; Salaneck, W. R. Electroluminescence in Conjugated Polymers. *Nature* **1999**, *397***,** 121-128.

[39] Jasieniak, J.; Padicifico, J.; Signorini, R.; Chiasera, A.; Ferrari, M.; Martucci, A.; Mulvaney, P.Luminescence and Amplified Stimulated Emission in CdSe–ZnS-Nanocrystal-Doped TiO2 andZrO2 Waveguides. *Adv. Funct. Mater.* **2007**, *17*, 1654.-1662.

[40] Pang, L.; Shen, Y.; Tetz, K.; Fainman, Y. PMMA Quantum Dots Composites Fabricated via Use of Pre-polymerization. *Opt. Express*. **2005**, *13*, 44-49.

[41] Suárez, I.; Gordillo, H.; Abargues, R.; Albert, S.; Martínez-Pastor, J. Photoluminescence Waveguiding in CdSe and CdTe QDs-PMMA Nanocomposite Films. *Nanotechnology* **2011**, *22*, 435202-8.

[42] Wang, M.; Zhang, M.; Qian, J.; Zhao, F.; Shen, L.; Scholes, G.; Winnik, M. Enhancing the Photoluminescence of Polymer-Stabilized CdSe/CdS/ZnS Core/Shell/Shell and CdSe/ZnS Core/Shell Quantum Dots in Water through a Chemical-Activation Approach. *Langmuir* **2009**, *25*, 11732-11740.

[43] Sundar, V. C.; Eisler, H. J.; Bawendi, M. G. Room-Temperature, Tunable Gain Media from Novel II–VI Nanocrystal–Titania Composite Matrices. *Adv. Mater*. **2002**, *14*, 739-743.

[44] Petruska, M. A.; Malko, A. V.; Voyles, P. M.; Klimov, V. I. High-Performance, Quantum Dot Nanocomposites for Nonlinear Optical and Optical Gain Applications. *Adv. Mater*, **2003**, *15*, 610-613.

[45] Chandler, R. E.; Houtepen, A. J.; Nelson, J.; Vanmaekelbergh, D. Electron Transport in Quantum Dot Solids: Monte Carlo Simulations of the Effects of Shell Filling, Coulomb Repulsions, and Site Disorder. *Phys. Rev. B* **2007**, *75*, 085325-10.

[46] Hines, M. A.; Scholes, G. D. Colloidal PbS Nanocrystals with Size-Tunable Near-InfraredEmission: Observation of Post-Synthesis Self-Narrowing of the Particle Size Distribution. *Adv.Mater.* **2003**, *15*, 1844–1849.

[47] Yu, W. W.; Peng, X. Formation of High-Quality CdS and Other II – VI SemiconductorNanocrystals in Noncoordinating Solvents: Tunable Reactivity of Monomers. *Angew. Chem.* **2002**, *114*, 2474-2477.

[48] Kinder, E.; Moroz, P.; Diederich, G.; Johnson, A.; Kirsanova, M.; Nemchinov, A.; O'Connor, T.; Roth, D.; Zamkov, M. Fabrication of All-Inorganic Nanocrystal Solids

through Matrix Encapsulation of Nanocrystal Arrays. *J. Am. Chem. Soc.* **2011**, *133*, 20488-20499.

[49] Pathan, H. M.; Lokhande, C. D. Deposition of Metal Chalcogenide Thin Films by Successive Ionic Layer Adsorption and Reaction (SILAR) Method. *Bull. Mater. Sci.* **2004**, *27*, 85-111.

[50] Semonin, O. E.; Johnson, J. C.; Luther, J. M.; Midgett, A. G.; Nozik, A. J.; Beard, M. C. Absolute Photoluminescence Quantum Yields of IR-26 Dye, PbS, and PbSe Quantum Dots *J. Phys. Chem. Lett.* **2010,** *1,* 2445-2450.

[51] Manna, L.; Scher, E. C.; Li, L.-S.; Alivisatos, A. P. Epitaxial Growth and Photochemical Annealing of Graded CdS/ZnS Shells on Colloidal CdSe Nanorods. *J. Am. Chem. Soc.* **2002**, *124*, 7136– 7145.

[52] Carbone, L.; Cozolli, P. D. Colloidal Heterostructured Nanocrystals: Synthesis and Growth Mechanisms. *Nano Today,* **2010,** *5*, 449-493.

[53] Donega, C. D. Synthesis and Properties of Colloidal Heteronanocrystals. *Chem. Soc. Rev.***2011**, 40, 1512– 1546.

[54] Moroz, P.; Kholmicheva, N.; Mellott, B.; Liyanage, G.; Rijal, U.; Bastola, E.; Huband, K.; Khon, E.; McBride, K.; Zamkov, M. Suppressed Carrier Scattering in CdS-Encapsulated PbS Nanocrystal Films. *ACS Nano* **2013**, *7*, 6964-6977.

[55] Helms, V. Fluorescence Resonance Energy Transfer". Principles of Computational Cell Biology. Weinheim: Wiley-VCH. p. 202. 2008.